Environmental Advances 15 (2024) 100453

Contents lists available at ScienceDirect

Environmental Advances

journal homepage: www.sciencedirect.com/journal/environmental-advances

Potentially toxic elements speciation in bottom ashes from a municipal solid waste incinerator: A combined SEM-EDS, μ-XRF and μ-XANES study

C. De Matteis [a,*], S. Pollastri [b,c], L. Mantovani [a], M. Tribaudino [d]

[a] Dipartimento di Scienze Chimiche, della Vita e della Sostenibilità Ambientale (SCVSA), Università di Parma, 43124, Parma, Italy
[b] Elettra Sincrotrone Trieste S.C.p.A., 34149, Trieste, Italy
[c] Department of Physics, Computer Science and Mathematics, University of Modena and Reggio Emilia, Via Campi 103, 41125, Modena, Italy
[d] Dipartimento di Scienze della Terra, Università di Torino, 10124, Torino, Italy

ARTICLE INFO

Keywords:
Municipal solid waste incinerator bottom ash
Potentially toxic element
Chemical-mineralogical characterization
X-ray absorption near edge structure
Speciation
Leaching

ABSTRACT

Bottom Ashes from Municipal Solid Waste Incinerators and Waste to Energy plants represent an interesting source of secondary raw materials for many applications, like urban mining and inclusion in concrete, and road pavement. However, Bottom Ashes may contain potentially toxic elements, whose actual toxicity depends essentially on their oxidation state and mineralogical environment. For this reason, a representative sample of bottom ashes from Parma Waste to Energy plant has been selected to investigate the chemical speciation of Cr, Ni, Pb, Co, Zn and Cu by means of complementary techniques: Scanning Electron Microscopy with Energy Dispersive X-Ray Spectroscopy (SEM-EDS), micro X-Ray Fluorescence (μ-XRF) mapping and X-Ray Absorption Near Edge Structure (XANES) measurements by synchrotron radiation. This multi-technique approach allowed to obtain a general image of the mineralogical and chemical environment in which these elements are found. SEM-EDS analyses show the presence of Zn and Pb both in minerals and in glass matrix. Cr has been detected in the form of oxide and in spinel structure (chromite) whereas Co and Cu are found as alloy or metal inclusions. μ-XRF mapping reveals that Cu, Ni and Cr are generally associated to Na, K and Si suggesting their presence in glass matrix. XANES investigations exhibit that Cu has a variable oxidation state that suggesting its presence in the form of oxide, hydroxide, acetate and metal. Zn is mainly found as +II and in a number of different phases (including Zn-carbonates, in agreement with SEM-EDS data). Cr has been found only as +III, with XANES features resembling those of chromite, whereas as +VI was never identified. Ni and Co were found either as metal form and oxides. Pb spectra show a good match with oxides.

1. Introduction

A considerable input of anthropogenic material in the environment is given by waste. In 2016, global waste production reached 2.01 billion tons, and due to demographic and economic increase, it is estimated that this will increase to 3.40 billion tons by 2050 (Kaza et al., 2018).

The waste can be sent to recycling, composting, incineration processes or disposed in landfills. A considerable amount of waste, as much as 11 % of the global production, is incinerated (Kaza et al., 2018). In developed nations, the process of incineration takes place in Waste-to-Energy (WtE) facilities. These facilities harness energy by efficiently burning Municipal Solid Waste (MSW), generating both heat and electricity through controlled combustion.

Fly Ashes (FA) and Bottom Ashes (BA) are the main products of WtE processes. FA are categorised as hazardous waste and constitute 4 % of MSW mass, while BA are currently classified as a non-hazardous waste and represent 20 % of MSW mass (Bertolini et al., 2004; Izquierdo et al., 2001; ANPA, 2002).

BA are constituted by an extremely complex and heterogeneous mineral and glassy fraction. In recent years, several studies addressed the characterization of BA from a chemical, geochemical, mineralogical and physical point of view (Alam et al., 2019; Assi et al., 2020; Bayuseno and Schmahl, 2010; Caviglia et al., 2019; Huber et al., 2020; Loginova et al., 2019; Mantovani et al., 2021).

BA contain silicates, carbonates, hydrated minerals, sulphates, phosphates, oxides and an amorphous component that in the larger particle size classes can be up to 80–90 % of the global content (Alam et al., 2019; Assi et al., 2020; Bayuseno and Schmahl, 2010; Caviglia

* Corresponding author.
E-mail address: chiara.dematteis@unipr.it (C. De Matteis).

https://doi.org/10.1016/j.envadv.2023.100453
Received 20 June 2023; Received in revised form 7 November 2023; Accepted 13 November 2023
Available online 22 November 2023

et al., 2019; Inkaew et al., 2016). The major elements are Si, Ca, Al, Mg, Fe, K, S, P and Na whereas among the minor, few Potentially Toxic Elements (PTE) such as Ni, Cu, Cr, Zn and Pb can be found (Alam et al., 2019; Caviglia et al., 2019; Funari et al., 2015; Mantovani et al., 2021).

With respect to the global Earth crust composition, Dijkstra et al. (2019) showed an enrichment in Ca, S and P, and slightly less in Si; however, it is important to note that PTE are strongly enriched with respect to the Earth Crust (Tribaudino et al., 2023). This bias arises when attempting to reuse BA, as it may lead to the potential release of PTE into the environment. PTE have earned the moniker "chemical time bombs" due to their resistance to biodegradation and their extended presence in soil (De Silva et al., 2021; Stigliani et al., 2010). High PTE contents cause decreases fertility in soil, degeneration of the ecosystem, and reduction productivity in crop (Xu et al., 2017). PTE can also manifest their toxic and carcinogenic effects when they get into agricultural products, animals, and human bodies, thereby posing environmental risks that ultimately threaten both human health and ecological stability (Lei et al., 2016). As BA are recycled in road based applications (Bawab et al., 2021), there is a potential risk for soil and water contamination. Therefore, it is crucial to have a comprehensive understanding of the behavior of PTE present in these materials.

Several investigations on the leaching behaviour of BA were done, demonstrating that PTE release is major in finer grain size because of both the particle dimension and the greater presence of water-soluble mineralogical phases such as ettringite and hydrocalumite (Alam et al., 2019; Caviglia et al., 2019; Feng et al., 2007; Huber et al., 2020; Loginova et al., 2019; Mantovani et al., 2021; Šyc et al., 2020; Wei et al., 2017; Yao et al., 2012).

The mobility of an element to an environmental matrix is strictly connected to mineralogical and chemical characteristics: PTE in silicates or glasses are released only after a strong acid attack, whereas PTE in soluble phases may be easily released in the environment. Therefore, several authors carried out sequential extractions to investigate the association between elements, crystalline or amorphous phases and their leaching behaviour (Abramov et al., 2018; Alam et al., 2019; Goodarzi and Huggins, 2001; Haberl and Schuster, 2019; Zhu et al., 2018).

However, due to the complexity of the material and the relatively low concentration of PTE, it is difficult not only to obtain an unambiguous correspondence between mineralogical and chemical information but also to analyse the PTE at a detailed scale, determining their concentration and oxidation state in the different phases. This information is crucial to predict and assess the potential release and toxicity, but also for a valuable reuse of BA (Rissler et al., 2020).

Synchrotron-based X-Ray Absorption Spectroscopy (XAS) is among the main techniques used to investigate the chemical speciation of elements. The main advantage of XAS is represented by its chemical selectivity for the determination of the local atomic environment and oxidation state of a given element. It is a very sensitive method, able to investigate elements also in low concentration (ppm down to ppb, depending on the beamline characteristics).

In literature, the use of synchrotron-bases XAS for MSWI investigation is reported only in few studies. Most data focused on Cu and Zn speciation in FA (Hsiao et al., 2006, 2002, 2001), less on BA (Lassesson and Steenari, 2013; Rissler et al., 2020; Steenari and Norén, 2008; Tiberg et al., 2021) and no data are available on other critical elements like Pb, Cr and Ni.

A limit in XAS method is the lack of analytical data on the other elements present in the same analytical point. Therefore, textural information, like crystal size, clustering, shape and/or inclusions of other phases in the areas of analysis is lost. This affects the reliability of the XAS analyses in showing the distribution of the different phases in the sample. Synchrotron radiation-based μ-XANES together with μ-XRF provides a powerful alternative. With a narrowly focused beam, sized as little as $50 \times 50 \mu m^2$, μ-XRF mapping shows the local composition, with a sensitivity down to the ppm for the minor elements. The distribution of the PTE can be revealed, and in selected points the XANES spectra can be acquired to determine the local environment for specific elements.

μ-XRF and XANES were already combined for environmental and cultural heritage studies, where an heterogeneous matrix is present (Kostomitsopoulou Marketou et al., 2021; Liu et al., 2020), but not for BA from WtE plants yet.

Hence, in order to fulfill this gap, a representative sample of BA from Parma WtE plant with particle size 0.5–1mm, has been selected to be investigated throughout a multi-technique approach, combining SEM-EDS, μ-XRF and μ-XANES data. A preliminary mineralogical and chemical characterization of the bulk material (X-Ray Powder Diffraction, XRPD, and lab-based XRF) was also carried out on the same grain size.

The novelty of the present study is to report for the first time combined μ-XRF and XANES data on BA, aiming at the determination of not only the chemical form and speciation of PTE, but also their textural distribution and association with other elements. SEM-EDS analyses have been performed on the same studied sample, as well. In respect with μ-XRF, the analytical resolution of SEM-EDS analysis is lower, being not possible to reveal elements below 0.1 wt%; however, a much better spatial resolution is present, analysing an area as low as 1 μm^2, with an even better resolution in imaging.

2. Materials and methods

2.1. Sample description

The BA samples come from Parma WtE plant (northern Italy), property of Iren Ambiente S.p.A. The plant operates since 2014 and has an authorized disposal capacity of 160.000 t/y of waste. The materials treated are MSW and non-hazardous special waste (Iren Ambiente, 2022). WtE plant has a grate furnace technology and burns at about 1000°C. BA were taken from 2-3m high stockpile in May 2019.

BA were mixed, dried in an oven at 60°C for 24 h and sieved. The 0.5-1mm grain size was selected to conduct this study and then, to have a more representative sample, it was quartered. The bulk composition of this grain size was measured by XRF (Mantovani et al., 2021). The results are shown in Table 1.

About 1 g of sample was used for XRPD analyses, while another part of sample was embedded in epoxy resin and cut longitudinally to obtain a polished section for SEM-EDS, synchrotron XRF and XANES analyses. The stab was $2 \times 2 cm^2$. A selected area of the stab was chosen and a chemical map with SEM-EDS was acquired (Fig. 1); within this selected area, four smaller areas were selected for XRF mapping and XANES measurements.

2.2. X-ray powder diffraction analyses

XRPD measurement was performed with a Bruker D2 Phaser powder diffractometer, operating with Cu Kα ($\lambda = 1.54178$ Å) radiation at 30 kV and 10 mA. The diffraction patterns were done in the 5-100° 2θ range, with a 0.02°/sec for step. The diffractometer had a θ-θ focalizing geometry and solid state detector. A sample rotation of 30 rpm was applied to avoid crystal preferential orientation effects. Identification of the diffraction patterns were done using DIFFRAC.EVA software (Bruker, Germany). The Crystallography Open Database (COD) and the ICDD PDF-2 database were used for phase identification.

Rietveld analysis GSAS 2 software package (Toby and Von Dreele, 2013) was used (Gualtieri, 2000; Pagani et al., 2010) to quantify the major crystalline phases and the amorphous material; a 10 % Al_2O_3 corundum was used as standard. XRPD results are reported in Table 2.

2.3. SEM-EDS

The SEM-EDS analyses were performed on a 2.0×0.8 cm^2 slice, using a JEOL JSM-IT 300LV Scanning Electron Microscope, equipped with Oxford INCA Energy 200 EDS SATW detector (WD 10, KV 15), at 15kV, 1.2mA current and 1μm beam diameter. The data were collected

Table 1
X-Ray Fluorescence (XRF) analysis of major, minor and trace elements for the BA of 0.5–1mm grain size from WtE of Parma. Minor and trace elements are in mg/kg while major elements are expressed as g/100g of their oxides and loss of ignition (LOI) values %.

Major Elements (g/100g)	
SiO_2	29.20
TiO_2	0.92
Al_2O_3	8.96
Fe_2O_3	3.48
MnO	0.10
MgO	3.59
CaO	28.41
Na_2O	2.18
K_2O	1.29
P_2O_5	2.19
LOI	19.69
Minor Elements (mg/kg)	
As	56
Ba	1618
Ce	36
Cl	10120
Co	57
Cr	697
Cu	1885
Ga	14
Hf	< 3
La	21
Mo	13
Nb	10
Nd	20
Ni	179
Pb	802
Rb	27
S	14780
Sc	13
Sn	43
Sr	517
Th	7
U	< 3
V	79
Y	14
Zn	5750
Zr	169

and processed using the AZTEC software (Oxford Instrument). The mapping was done on 33 frames, which were subsequently merged, each with a 1024 × 768 pixel resolution, under a 50 times magnification, dwell time 1500μsec. The whole collection lasted about 14 hours. Each analytical point sized 2.5 μm^2.

2.4. Synchrotron radiation

μ-XRF mapping and XANES measurements were conducted at Elettra synchrotron radiation source, at the 10.1L XRF beamline (Jark et al., 2014; Karydas et al., 2018; Wrobel et al., 2016). The experiment was performed using both HE multilayer (for the collection of XRF maps) and Si111 (for the collection of XANES spectra) monochromators, with standard 45°/45° geometry for fluorescence mode measurements, and an X-Flash 5030 SDD detector (Bruker, Berlin, Germany). A pair of parallel plane mirrors intercepting the beam in grazing incidence suppressed higher order harmonics contaminations.

The flat surface of the bottom ashes sample embedded in epoxy resin has been mounted on a Teflon sample holder, with also reference metal foils mounted on the side (perpendicularly) for energy calibration of the monochromator (in transmission mode, using a Hamamatsu Si-photodiode S3590-09, 10 × 10 mm^2, 300μm thickness) prior to XANES measurements.

XRF maps were collected with an incident beam energy of 14 keV and a beam size at the exit slits of 50 × 50 μm^2 (H x V).

XANES spectra at the K-edges of PTE Cr, Co, Ni, Cu and Zn (5989, 7709, 8333, 8979 and 9659 eV, respectively) and at the L3-edge of Pb (13035 eV) were collected on 37 points, which were chosen based on the higher content in PTE (Co, Cr, Ni, Cu, Zn and Pb) from μ-XRF maps.

All spectra were collected using a variable energy step as a function of the energy and 5 seconds per step: in the first 200 eV of the spectrum a large step (5 eV) and a smaller step (0.2 eV) in the near-edge region. Above the absorption edge a k-constant step of 0.05 $Å^{-1}$was used.

In order to increase the signal to noise ratio, multiple spectra were collected and merged. The oxidation state was determined using least-squares Linear Combination Fitting (LCF) based on reference spectra collected on compounds of known oxidation state (either provided by

Table 2
Rietveld refinement for quantitative mineralogical composition of the major phases in the examined grain size (0.5 – 1mm); in addiction, some phases with low of doubtful content are only reported as **X**: present, but not refined, * dubious.

Mineral Phase	Formula	Wt%
calcite	$CaCO_3$	8 (1)
vaterite	$CaCO_3$	2 (1)
quartz	SiO_2	3 (1)
melilite	$(Ca, Na)_2(Mg, Fe, Al, Si)_3O_7$	2 (1)
plagioclase	$(Ca,Na)[Al(Al,Si)Si_2O_8]$	2 (1)
strätlingite	$Ca_2Al_2SiO_7{\cdot}8H_2O$	2 (1)
ettringite	$Ca_6Al_2(SO4)_3(OH)12{*}26H_2O$	3 (1)
hydrocalumite	$Ca_4Al_2(OH)_{12}\ (Cl,CO_3,OH)_2{\cdot}4H_2O$	3 (1)
hematite	Fe_2O_3	3 (1)
magnetite	$Fe^{2+}Fe_2^{3+}O_4$	< 3 (1)
amorphous		72 (6)
larnite	Ca_2SiO_4	x
portlandite	$Ca(OH)_2$	x
tobermorite	$Ca_4Si_6O_{17}(H_2O)_2{\cdot}(Ca{\cdot}3H_2O)$	*
apatite	$Ca_5(PO_4)_3(Cl/F/OH)$	*

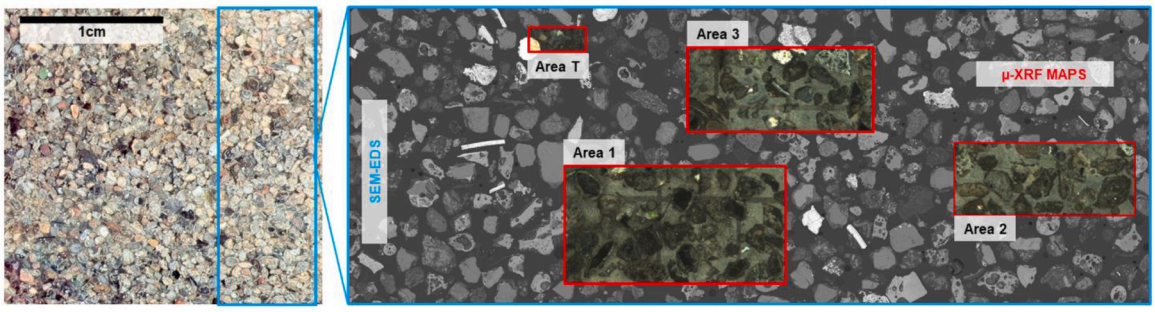

Fig. 1. Left: Image of the stab containing the polished grains of the bottom ashes, with the area where SEM-EDS analyses were performed (blue frame). Right: SEM backscattered electrons image of the same area, with red frames indicating the areas of XRF and XANES analyses as visible with the optical microscope available at the beamline. (For interpretation of the references to color in this figure legend, the reader is referred to the web version of this article.)

the beamline database or from the literature). Normalization of XANES spectra, background removal and LCF analyses were done using the Athena software package (Ravel and Newville, 2005).

3. Results

3.1. X-ray powder diffraction

XRPD results (Table 2) shows that amorphous material is the main component. As reported in Mantovani et al. (2021), in the analysis of BA from the same plant, the amorphous portion is on itself heterogeneous, showing areas more or less Fe and Ca rich. The amorphous fraction is made in part by residual glass, already in amorphous state before incineration (i.e. bottle glass), and in part by the melt during incineration. In the latter case it was found in local equilibrium with different crystalline phases.

Crystalline phases identified by XRD, in agreement with literature data, can be divided into three groups: a) phases like quartz, apatite and refractory materials which were present before combustion, b) phases like melilite, anorthite, magnetite, and hematite which are formed during combustion, or c) phases formed during the quenching and the subsequent aging of the ashes, as carbonates (calcite and vaterite), and a number of typical cementitious materials phases (Bayuseno and Schmahl, 2010; Bourtsalas et al., 2014; Chimenos et al., 2003; Eusden et al., 1999; Inkaew et al., 2016; Piantone et al., 2004; Santos et al., 2013; Wei et al., 2011; Zevenbergen et al., 1998). To note, the phases in

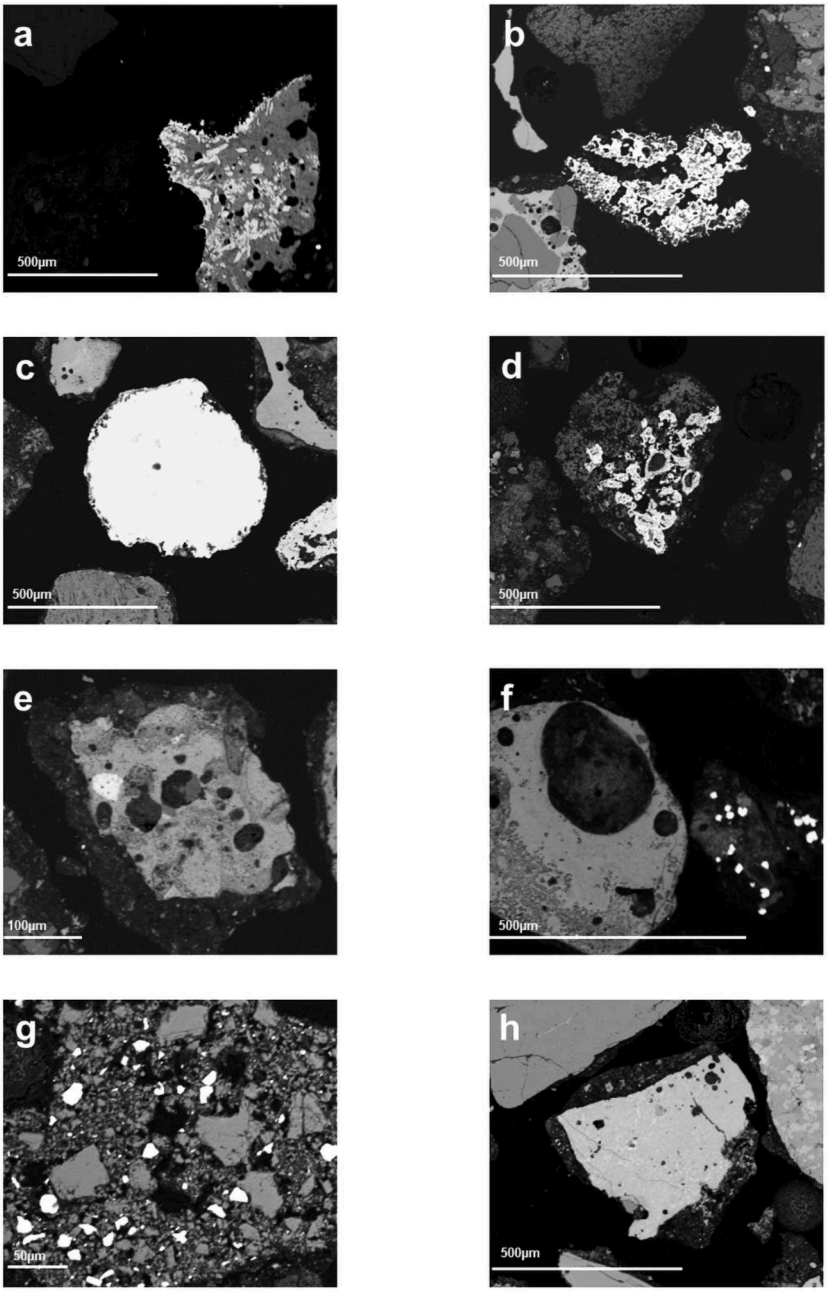

Fig. 2. SEM-BSE image of grains with PTE: a) Willemite-hardystonite assemblage (willemite white, hardistonite gray); b) ZnO (white), overgrowing non stoichiometric Zn bearing gehlenite (gray); c) Cu-Sn oxidized alloy (white); d) Zn-Mn oxide (white); on the left of the image we find Ca-carbonate, gray, and glass, dark gray; e) $FeCrO_3$, white, coexisting in a composite grain with Ca-rich glass (light grey) and alumina (dark gray round phases); f) Ca-plumbate (Ca_2PbO_4), shown by white squared grains, together with lime (light gray), and silicate glass; g) Pb with TiO_2 oxide (white rounded grains); h) glass matrix with Cr-oxide inclusions (white points).

which PTE are present as a main component, observed by XANES and SEM-EDS, were not revealed by XRPD since it is under detection limit for this technique.

3.2. SEM-EDS

SEM-EDS mapping was done to show where the critical elements (Zn, Cr, Ni, Pb, Cu, Co) are most concentrated, and where they form phases as major components, like zincates, plumbates or Cu alloy. Quantitative analyses were done on point and/or area of grains with higher concentration of PTE to determine the stoichiometric compositions. Due to the overlap of the strong L_α line of Zn with the K_α of Na, and of the M_α line of Pb with the K_α of S, K_α and L_α of Zn and Pb, respectively, were used to chart these elements.

Spatial resolution was another issue: in several cases the PTE-bearing phases could not be analysed due to the size of the crystals, below the spatial resolution of the SEM-EDS analysis. In few larger sized grains, it was possible to retrieve the composition without overlap of the neighbouring phases and to identify phases by stoichiometry. In Fig. 2 the images of a few grains including phases with PTE as major components, are shown.

As a rule, PTE are found in solid solution with more common elements, so that the stoichiometric mineral formula deviates from that of the pure mineral phase, as following.

Zn was found in a single grain as Mg-rich willemite. Willemite is a Zn orthosilicate, with stoichiometric formula Zn_2SiO_4, here with significant Mg content exchanging for Zn in solid solution. The Mg-willemite composition is $Zn_{1.74}Mg_{0.23}SiO_4$. It coexists with a Na-rich hardystonite $[(Ca_{1.7}Na_{0.3})(Mg_{0.1}Zn_{0.8}Al_{0.1})(Si_{1.9}Al_{0.1})O_7]$. (Fig. 2**a**). Hardystonite is a Zn-bearing melilite, with nominal composition $Ca_2ZnSi_2O_7$; in our sample there is a strong deviation from nominal composition, due to an exchange of Na for Ca, Mg and Al for Zn, and Al for Si. The willemite-hardystonite assemblage in the ZnO-CaO-SiO_2 system is stable below 1301°C, at which temperature it melts incongruently to zincite (ZnO) and melt (Shevchenko and Jak, 2019).

In another grain, zincite (ZnO) was found seemingly coexisting with a $Zn_4Al_2O_7$ phase, in a silica free environment. The $Zn_4Al_2O_7$ phase is reported after decarbonation of Zn, Al-carbonate (Pshinko et al., 2013); it is not expected to form starting from oxides, as in the Al_2O_3-ZnO phase diagram the intermediate phase between oxides is the gahnite spinel ($ZnAl_2O_4$) (Sharma and Yoo, 2018). Gahnite spinel is present in the same grain, but not mingled with ZnO. Zincite is also found in grains without coexisting phases, with stoichiometric composition, or in solid solution with Mn ($Zn_{0.43}Mn_{0.57}O$), in this case coexisting with glass and Ca-carbonate. Moreover, in one grain zincite crystals are found crowning non stoichiometric gehlenite, with composition $(Ca_{1.8}Mn_{0.2})(Zn_{0.3}Al_{0.7})(Si_{1.9}Al_{0.1})O_7$ (Fig. 2**b**).

SEM-EDS analysis revealed also several grains with Zn content up to 2 wt %, dissolved in Na- and Mg-rich silicate glass.

Cr is found in several grains as a background peak with concentration below 1 wt %. As a major constituent, Cr was observed in three grains: in one grain as stoichiometric $FeCrO_3$ oxide and in two others as chromite spinel ($FeCr_2O_4$), coexisting with glass. Both indicate the association with Fe, and the speciation in oxides (Fig. 2e and h).

Cu was found in one metal grain in alloy with Sn, without coexisting phases (Fig.2c). Partial oxidation is revealed by the presence of a small O peak. The measured stoichiometry, with O measured as a separate element, i.e. not constrained by cation stoichiometry, is $Cu_{0.73}Sn_{0.07}O_{0.20}$. In the same sample two small EDS peaks of Cl(K_α) and S(K_α) may indicate alteration to sulphate and chloride of the metals. Cu was also found in small sized metal drops throughout the sample.

Co was found in one metal grain, in alloy with Mo and in an alumina matrix. No grains containing Ni in a major amount were found.

Pb was generally too low to be revealed as major phase. In one grain it was found a Pb bearing phase, Ca-plumbate (Ca_2PbO_4), together with lime (CaO) and glass (Fig. 2f). The Ca_2PbO_4 phase was found in oxidizing conditions by Suzuki et al. (1998), and can be obtained by reaction of a Pb-bearing compound with lime. It is a phase soluble in hot water and decomposes in weakly acid environment, which might be a source of potential leaching (Jernejcic et al., 1969). On the other hand, Wang et al. (2016) report that the Ca-plumbate phase controls Pb volatilization during incineration.

3.3. Synchrotron-based μ-XRF

μ-XRF elemental maps (**Figures A, B, C**) show the distribution and relative quantities of the different elements (major and minor), together with the BSE and optical images of the investigated areas. μ-XRF results are here discussed together with morphological information from SEM-EDS.

The embedded grains are generally made by a core, with the shape neatly appearing from the epoxide in Backscattered Electrons (BSE) images. A rim usually borders the core, with smaller crystals embedded in a darker matrix. SEM-EDS analysis on the rims could be done just in few larger crystals, finding that they have a different composition than the core; the rims contain Ca-carbonate, phosphates, residual plagioclase, sulphates and chlorides.

μ-XRF maps show within the core of the grains, some elements, namely Ca and Si, but also Mg, Cr, Fe, Co, Al, Ti, P, and Pb are generally present. Cu and Zn are found both in the core and in the rims, whereas S and Cl and, to a lesser extent, K and Na, mostly at the rims. The different mineralogical composition between rim and the core grains suggests a formation of very small crystals of chloride and sulphate during weathering.

Leaching tests on the same sample showed that Cl and S are the most leachable, supporting the hypothesis of their presence at the rim of the grains, and not within silicate glasses.

Also, the core of the grains is heterogeneous: SEM-EDS observations at higher resolution indicate the coexistence of several crystals as silicates, oxides, carbonates, metals inclusions and glass (Fig. 2). μ-XRF data show a more detailed distribution of the PTE than SEM-EDS results: this is expected, as PTE are generally below SEM-EDS analytical resolution. However, in few cases when the μ-XRF indicates a higher concentration of a given element, it is not possible to find a counterpart in the SEM-EDS maps. Although the two methods analyse the same areas, the detected volume is different: in μ-XRF the beam probes a depth of few tens of microns, whereas the SEM-EDS probes 1-2 μm maximum. The PTE rich phase may not be present at the surface of the grain, so to be revealed by SEM-EDS, but just few microns below, and detected instead by μ-XRF.

Due to the spatial resolution of acquired μ-XRF maps, lower than that of SEM-EDS, and the heterogeneous nature of BA, a given μ-XRF analytical pixel may sample a number of different phases.

Throughout the overlaps of single elements μ-XRF maps, the distribution of PTE was analysed and associated to major elements (Si, Ca, Mg, Na, etc.) obtaining the mineralogical environment in which PTE are incorporated. Among the PTE, Cu is present generally together with Na, K and Si, in glass. To note, in the same areas EDS analysis do not revealed the presence of Cu-bearing phases, indicating that Cu is below the instrumental resolution or in tiny grains under the surface. Cu was found in one grain as a Cu-Sn alloy also with Ni; Cu was also found as alloy/metal inclusions and droplets dispersed within the glass as observed by Mantovani et al. (2021).

In a grain, Ni occurs in alloys with Co and Mn, and with Co and Cr. Generally, however, Ni appears together with Fe and Cr and, most frequently, together with Na, K, Si and Al in a glass. To note, Ni was not found together with S and Cl.

Co was found together with Ni, likely in alloy; overlap with O indicates some degree of oxidation. In the same grain, an overlap of Co and Cl might indicate formation of chlorides.

Cr is generally associated with Fe, but also with Si, Ca, Fe, Na and K. The suggestion is that it is dissolved in a glass, or in tiny chromite

crystals. Cr was not present together with S and Cl.

Pb is found most in larger grains, in the core and in the rims of the grains. It is associated with Ca and Zn, but not with Si. This could suggest a carbonate phase. Pb occurs with S in few grains, where S is present within the core. This is not unlikely, in view of the strong affinity of Pb for sulphides. Pb is also found with Si, Na, K and Mg in Pb-rich glass.

Zn is found in core as trace in amorphous material and in rims, together with S and Cl suggesting its presence in sulphates and chlorides. Zn was also found, together with Ti, in spinel-like structure.

3.4. XANES

A major advantage of XAS is to be element specific, modelling the X-ray Absorption Edge of a given electron transition for a given atomic species. It provides information on the local environment and oxidation state of the considered element, but it does not provide a precise chemical information of the specific phase where the element is present. As the element may be in different oxidation states and different phases within the area sampled by the beam, a deconvolution of the different contributions is often necessary. Combining XANES results with those from SEM-EDS and μ-XRF analysis, the disadvantage of not having the complete chemical composition of the emitting phase, is compensated by the sensitivity of the XANES, able to probe an element at few ppm concentrations and within submicrometric phases. Oxidation state and possible host phases for each of the PTE are here reported. Hereafter, the label of the spectra will be reported as *Xa_b* where *X* is the element, *a* is the area and *b* the point analysed.

3.4.1. Cobalt

XANES spectra were recorded at the Co K-edge in one clast, on which higher resolution SEM-EDS analysis showed that the grain is made by a partially oxidized Co-Mn alloy, mingled with Al_2O_3 and a Ca-silicate phase (Fig. 3).

XANES results confirm that Co is present in a partially oxidized alloy: LCF analysis indicates that 68 % of Co is present as a metal and 32 % as Co-oxide. In the same grain, a single XRF spectrum extracted from the map highlight the co-presence of Ni, that was below the analytical resolution of SEM-EDS. A XANES spectrum collected at the Ni K-edge (labelled as Ni3_1). indicates that also Ni is present as a partially oxidized alloy: LCF results shows that metal Ni (84 %) coexists with divalent Ni-oxide (16 %).

3.4.2. Copper

XANES spectra collected at the Cu K-edge in different clasts are reported in Fig. 4. LCF analysis (Table 3) suggests that Cu chemical environment and oxidation state are heterogeneous even in the same area, ranging from metallic to Cu +II.

Two spectra (Cu1_1and Cu2_2) have a broad white line peak at about 8997 eV, together with minor pre-edge peaks at about 8981 and 8985 eV, respectively. They fit with divalent Cu-oxide, but the contributions of monovalent Cu-oxide, and, in one spectrum, of residual metal, are necessary to obtain the best fit. In another grain (Cu3_1) we find a doublet at 8994 and 8998 eV, possibly indicating the presence of cupric acetate.

SEM-EDS analysis on the same areas did not show phases with sufficient enrichment in Cu to show significant emission in CuKα peaks. It is possible that Cu in the areas is below the analytical resolution of SEM-EDS, i.e. few thousands of ppm, but it could be also an effect of the different sampling size of SEM-EDS and XANES analyses. Only in one case Cu was found by SEM-EDS analysis as well, in a Cu-Ni-Sn alloy (Fig. 2**c**). In this grain, XANES spectrum fits with metal Cu (Cu_T in Fig. 4), showing the typical edge position and features at about 8994 and 9004 eV, and indeed confirmed by LCF results. The Cu speciation in BA showed that Cu is present in different oxidation states (0, +I and +II);

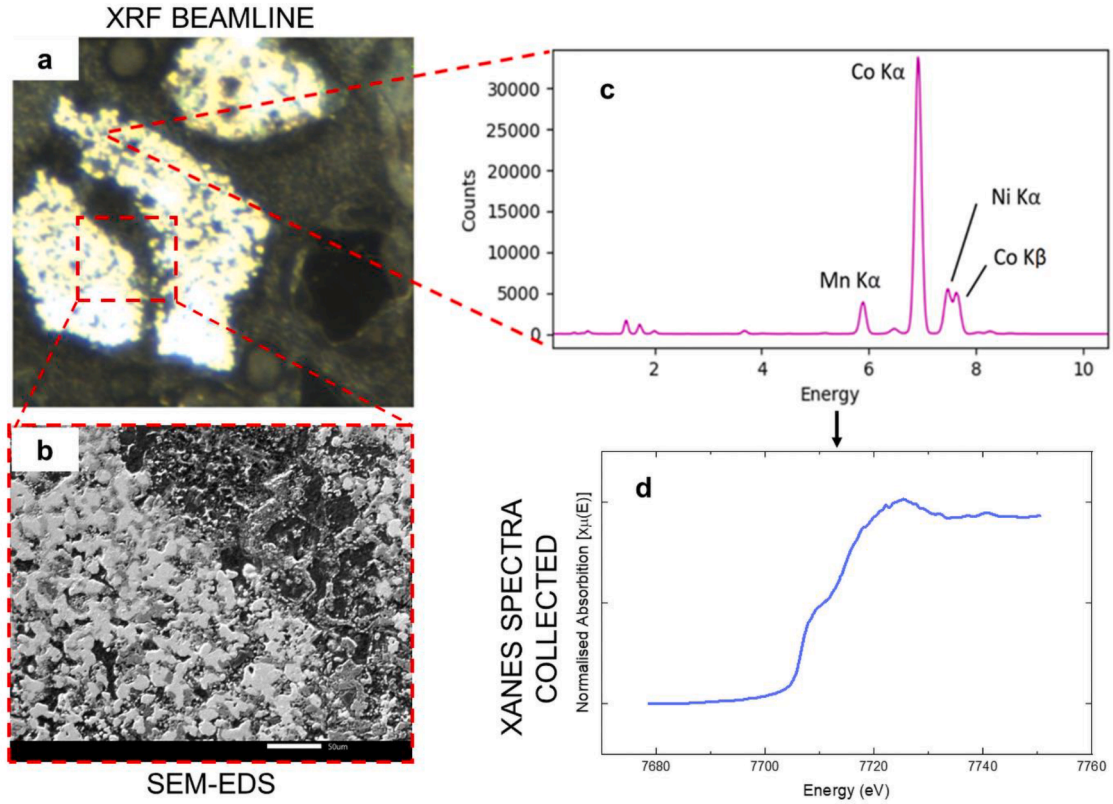

Fig. 3. Co-bearing grain. a) Image of the grain taken with the microcamera available at the XRF beamline; b) SEM-BSE image on the same area with a three phases assemblage: metal cobalt (white), oxidized area with Co/Mn ratio 2/1 (gray) and mixture of alumina and Ca-Al silicate (black); c) XRF spectrum representative of the clast, with label of the main fluorescence lines; d) Normalized XANES spectrum collected on the same grain at the Co K-edge.

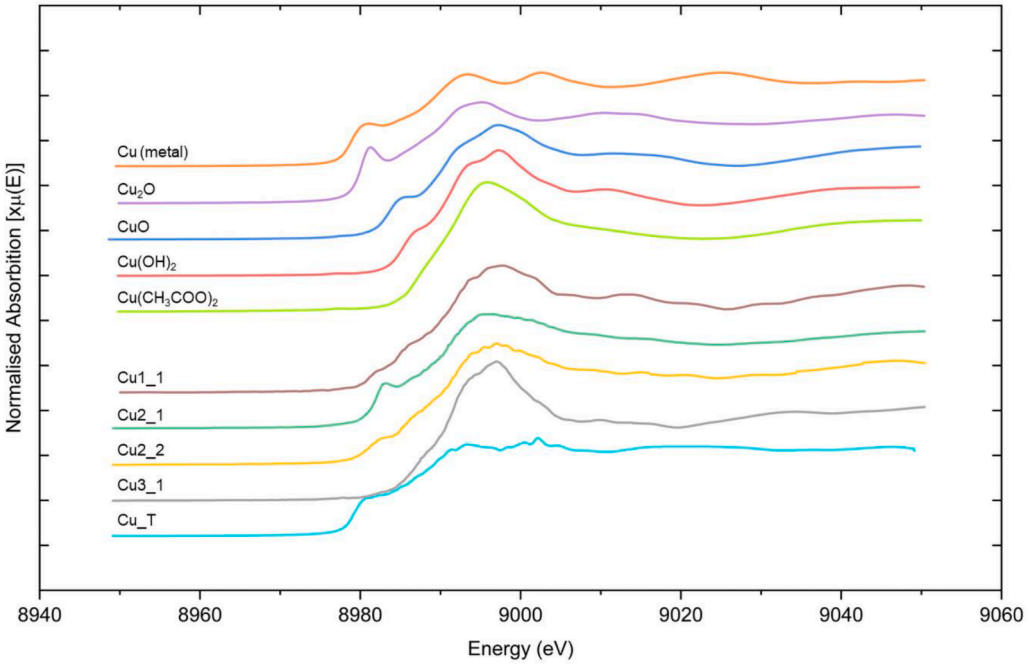

Fig. 4. Normalized Cu XANES spectra of reference materials (top) and collected on various clasts of the BA samples (bottom).

Table 3
Results of the LCF analysis performed on the spectra collected at the Cu K-edge on BA clasts (reported quantities are %; sigmas in brackets).

Compounds	*Cu1 1*	*Cu2_1*	*Cu2_2*	*Cu3_1*	*Cu_T*
Metal Cu		10 (4)			80 (3)
Cu_2O	6 (4)	24 (5)	13 (4)		16 (4)
CuO	94 (2)	66 (3)	87 (3)		4 (2)
$Cu(OH)_2$				11 (6)	
$Cu(CH_3COO)_2$				89 (6)	

this was also observed by Rissler et al. (2020), and interpreted as an effect of zones in the fuel bed with different access to the oxygen. Here, however, we observe coexistence of different oxidation states within the same grain.

3.4.3. Zinc

Zn was found in BA in a number of different phases, some of them well visible also in SEM-EDS. Various XANES spectra (12 in total) at the Zn K-edge were collected on different clasts; a selection of the most representative ones is reported in Fig. 5, where it is visible that the edge position of all the spectra is similar and shifted with respect to reference Zn foil, indicating that Zn is not present as a metal but mainly occurred in oxidation state +II (Table 4).

Clast Zn2_3 is the only one to have a weak pre-edge, whereas two peaks at about 9665.3 and 9667.9 eV are clearly distinguishable in all the spectra except that of clast Zn1_2, which has only one peak at about 9666.5 eV. The LCF proved difficult because of the heterogeneity of the collected spectra. In all the spectra, a great fit is obtained with Zn-carbonate, in the form of smithsonite ($ZnCO_3$) or hydrozincite ($Zn_5(CO_3)_2(OH)_6$). Smithsonite is here first observed, but Zn in solid solution within carbonate was reported by Piantone et al., (2004) in an investigation on weathering phases. Hydrozincite was found by Rissler et al. (2020) and dubiously by EXAFS analysis by Tiberg et al. (2021). Zincite (ZnO) was found in few grains, confirming SEM-EDS results and previous XAS data by Rissler et al. (2020) and Tiberg et al. (2021).

Due to the similarity of the XANES spectra of zincite and Zn-hydroxide, $Zn(OH)_2$ could be also present. In five of the examined spectra the fit required the ZnS phase in substantial amount. The phase is

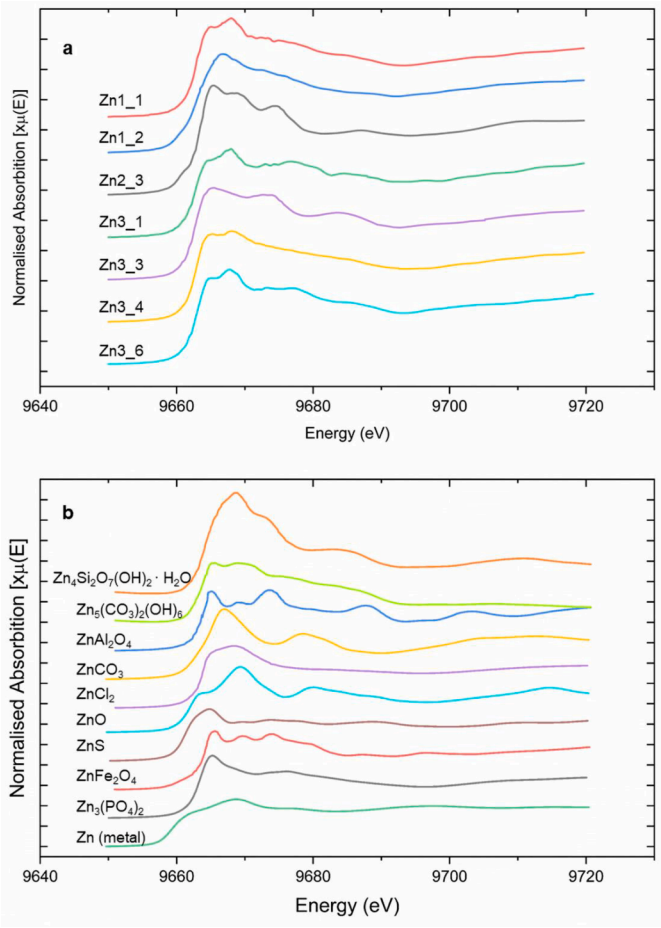

Fig. 5. Normalized Zn XANES spectra of reference materials (b) and seven selected spectra of BA samples (a). $Zn_4Si_2O_7(OH)_2 \cdot H_2O$, $Zn_5(CO_3)_2(OH)_6$, $ZnAl_2O_4$, $ZnCl_2$ and $ZnFe_2O_4$ spectra have been extracted from Rissler et al. (2020) using the free online tool WebPlotDigitizer (Rohatgi, 2014).

Table 4
Results of the LCF analysis performed on the spectra collected at the Zn K-edge on BA clasts (reported quantities are %; sigmas in brackets).

Compounds	*Zn1_1*	*Zn1_2*	*Zn1_3*	*Zn2_1*	*Zn2_2*	*Zn2_3*	*Zn3_1*	*Zn3_3*	*Zn3_4*	*Zn3_5*	*Zn3_6*	*ZnT*
ZnO				29 (6)			32 (5)	36 (6)				28 (6)
ZnS	27 (3)	51 (3)	33 (3)						54 (2)	62 (2)	51 (2)	
$ZnCO_3$		15 (2)		45 (7)	39 (4)	44 (3)	28 (4)	21 (5)				64 (6)
$ZnAl_2O_4$						34 (3)						
$Zn_4Si_2O_7(OH)_2 \cdot (H_2O)$							41 (6)		17 (3)	9 (3)	24 (5)	
$Zn_3(PO_4)_2$	42 (4)		41 (5)		27 (10)							
$ZnFe_2O_4$					34 (7)			43 (4)				
$Zn_5(CO_3)_2(OH)_6$	31 (5)	34 (0.9)	26 (1)			22 (4)			29 (4)	29 (4)	26 (2)	
$ZnCl_2$				26 (10)								8 (2)

here first observed, and could be present by reduction of sulphates during weathering. The presence of Zn-phosphate is not surprising, as several Zn phosphate phases were found by Piantone et al. (2004). However, Zn-phosphate was not found by Rissler et al. (2020). Also, spinel phases like gahnite and Zn-ferrite ($ZnFe_2O_4$) are present, as well as the silicate hemerophyte [$Zn_4Si_2O_7(OH)_2 \cdot H_2O$]. Both are common findings in Rissler et al. (2020), and Tiberg et al. (2021). However, a possible misinterpretation can be due to the absence of a standard for Zn in silicate glass, where it was found here and in Mantovani et al. (2021). Last, $ZnCl_2$ was found only in one spectrum (Zn2_1); this compound was found mainly in FA (Cai et al., 2015; Kitamura et al., 2020) but also in BA where its presence can be explained by the encapsulation of chloride within sintered BA particles (Rissler et al., 2020).

3.4.4. Chromium

The LCF analysis showed that three of the four collected spectra (Cr1_1, Cr2_1, Cr2_2) fit mainly with $FeCr_2O_4$, with a percentage ranging from 60–77 % (Table 5 and Fig. 6). In the spectra Cr1_1 and Cr2_1 metal Cr was also found (23 % and 27 %, respectively) and 40 % of Cr_2O_3 in Cr2_2. In one spectrum (Cr3_1) metal Cr (24 %) and Cr_2O_3 (76 %) were found, in agreement with SEM-EDS analytical results of chromium-aluminium oxide ($Cr_{1.81}Al_{0.19}O_3$). In all XANES spectra Cr was present in the Cr 0 and Cr III+ oxidation state. No evidence of Cr VI+, which would show the typical high intensity pre-edge peak at about 5993 eV, was found.

3.4.5. Lead

Several XANES spectra at the Pb L_3-edge were collected, which show the same features and are almost identical: a very broad white line peak at 13052 eV is invariably present (Fig. 7). From the comparison of the edge position with Pb metal foil and Pb oxide standard compound spectra, Pb is expected to be oxidized in all the clasts. The LCF analysis showed fits with $PbCO_3$ (29–43 %) and Pb_3O_4 (57–71%) (Table 6). In these compounds, Pb is present in +II and +III chemical forms. Other reference compounds, like PbO, PbO_2, and $PbCl_2$ were tested, but none gave a satisfactory fitting. Also, in the same areas, S fluorescence lines were not detected, which discarded PbS and $PbSO_4$ as possible candidates. As for Zn, we did not fit Pb in a glassy environment, so we cannot rule out the presence of Pb in an alkali rich silicate glass, which could be compatible with the chemical composition of some of the investigated clasts (from XRF data). XANES spectra of Pb in PbO-Ga_2O_3 glasses show, similarly to our sample, a single broad white line peak, which is also similar to the XANES spectrum of Pb in a silicate structure (Choi et al., 1999; Dubrail et al., 2009).

Table 5
Results of the LCF analysis performed on the spectra collected at the Cr K-edge on BA clasts (reported quantities are %; sigmas in brackets).

Compounds	*Cr1_1*	*Cr2_1*	*Cr2_2*	*Cr3_1*
Metal Cr	23 (3)	27 (1)		24 (2)
$FeCr_2O_4$	77 (3)	73 (1)	60 (4)	
Cr_2O_3			40 (4)	76 (1)

3.4.6. Nickel

Like Cu, Ni is found in SEM-EDS only in the above described grain together with Co, and is revealed just by XRF. The XANES spectra at the Ni K-edge (Fig. 8) were compared with Ni metal foil, NiO and $Ni(OH)_2$.

LCF analysis shows that Ni, like Cu and Co, is present in metal and oxidized form, but hydration is also possible. The results of LCF analysis (Table 7) indicate that the metal is always partially oxidized and hydrated.

4. Discussion

4.1. The fate of PTE

In previous investigations on the speciation of PTE, several potential host minerals were suggested (Crannell et al., 2000; Dijkstra et al., 2006; Dubrail et al., 2009; Mantovani et al., 2021; Olsson et al., 2009; Piantone et al., 2004; Rissler et al., 2020; Steenari and Norén, 2008; Tang et al., 2015; Tiberg et al., 2021; Wei et al., 2011a). Their results, together with the mineral phases found in this work are reported in Table 8, which shows a comprehensive list of the mineral phases found in bottom ashes and containing PTE. Notably, the presence of silicate glasses as major phases in the BA suggests the likelihood of significant speciation occurring in glassy phases. Within the BA, where local equilibria are prevalent, glasses with variable compositions, typically enriched in alkalis (Mantovani et al., 2021), can potentially host different atomic species within their structure. The glass formed at high temperatures in combustion chamber is easily identifiable in BSE images: it occurs in the core of grains, encases crystals, and exhibits a composition resembling Ca-Al silicate enriched in alkalis. This compositional pattern was also evident in XRF analyses, where SEM-BSE images showed the presence of glass. SEM-EDS analyses made on the grains core show the presence of Zn, Cr, or Pb in a glass matrix, albeit their content is closed to the detection limits. These elements were investigated with XANES, but the lack of reference standard spectra for PTE in amorphous matrix biases the interpretation of the spectra.

The characterisation of the heterogeneous matrix, mingling crystalline phases with a non-definite chemical composition, is challenging. Even with the combination of μ-XRF and SEM-EDS analyses, in only a few grains the phases hosting the investigated PTE were uniquely identified. Previous investigations (Rissler et al., 2020; Tiberg et al., 2021), without the use of μ-XRF, interpreted XANES spectra solely with crystalline phase standards, potentially overlooking the contribution of glass to the speciation. Taking into account these considerations, we can propose here a speciation for each PTE.

The most commonly observed form for Cu is that of a metal, which may undergo partial alteration to Cu I+ or Cu II+ oxides or $Cu(OH)_2$. The carbonate form, frequently seen in the alteration of mining deposits, is less reported. In a few cases it may be incorporated into the complex spinel oxide structure. Cu associated with silicates was not detected in this work, but it has been reported by Rissler et al. (2020) and Meima and Comans (1999). If present, Cu-silicates, together with metal Cu, are likely combustion products, while other forms are related to subsequent weathering. Literature data show that the elevated level of Cu can

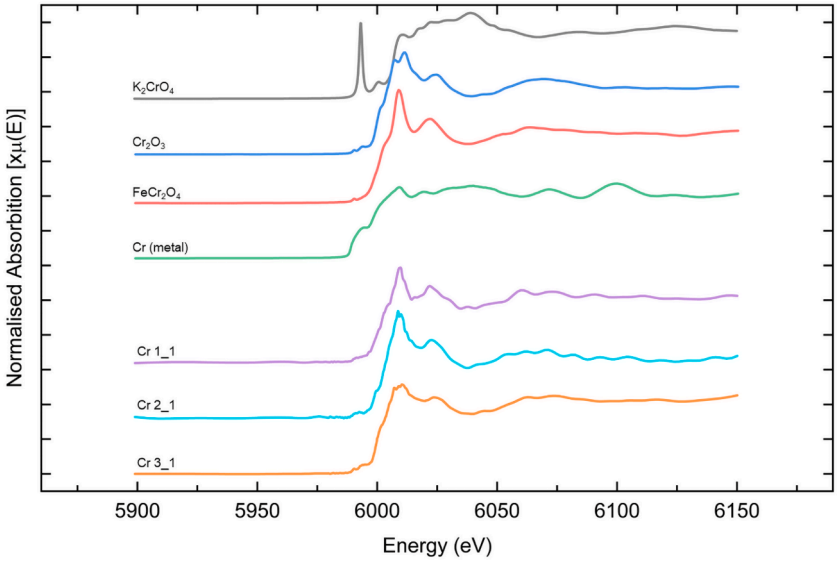

Fig. 6. Normalized Cr XANES spectra of reference materials (top) and collected on various clasts of the BA samples (bottom).

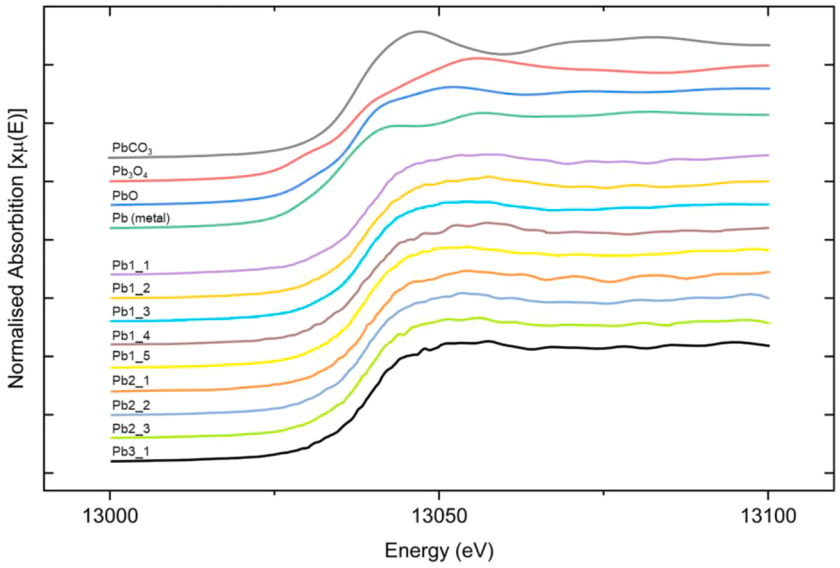

Fig. 7. Normalized Pb XANES spectra of reference materials (top) and collected on various clasts of the BA samples (bottom).

Table 6
Results of the LCF analysis performed on the spectra collected at the Pb L_3-edge on BA clasts (reported quantities are %; sigmas in brackets).

Compounds	*Pb1_1*	*Pb1_2*	*Pb1_3*	*Pb1_4*	*Pb1_5*	*Pb2_1*	*Pb2_2*	*Pb2_3*	*Pb3_1*
$PbCO_3$	31 (5)	29 (5)	40 (4)	25 (5)	43 (4)	29 (5)	38 (5)	37 (5)	29 (5)
Pb_3O_4	69 (5)	71 (5)	60 (4)	75 (5)	57 (4)	71 (5)	62 (5)	63 (5)	71 (5)

involve severe ecological implication (Aminiyan et al., 2018). In BA, Chen et al. (2020) show that Cu was very unstable and extremely easy to migrate. In this work, Cu is found in different oxidation states, primarily occurring as metal forms, pure or as alloys, with partial oxidation to Cu I+ and Cu II+. Tiny droplets of Cu were observed in silicate glasses. This work and Rissler et al. (2020) suggest that Cu may also undergo weathering as a hydroxide or a chloride.

No indications about the speciation of Co were found in the previous literature. Here, Co is predominantly present as alloys, often with Mn, Ni, or Fe, and only partially oxidized to Co II+.

An increase in Pb values in environmental matrices has already been observed by Patterson in 1965 due to the rise in industrial activities. More recently, it has been noted that high Pb levels can contribute to water, soil, and air pollution, and cause harm to living organisms due to bioaccumulation. To note, in the work of Astrup et al., (2016) the values of Pb in BA range from 75 to 14000 mg/kg encouraging a mindful reuse of this anthropogenic material. In literature, Pb was found as a major component in oxides, as an impurity in silicate glass or as an impurity in carbonates and ettringite (Table 8). In this work, Pb is mainly distributed in larger grains, both in the core and rim of glasses and carbonates, consistent with XANES results. Additionally, SEM investigation revealed Pb in the form of a Ca-plumbate phase, possibly formed by Pb-rich glass

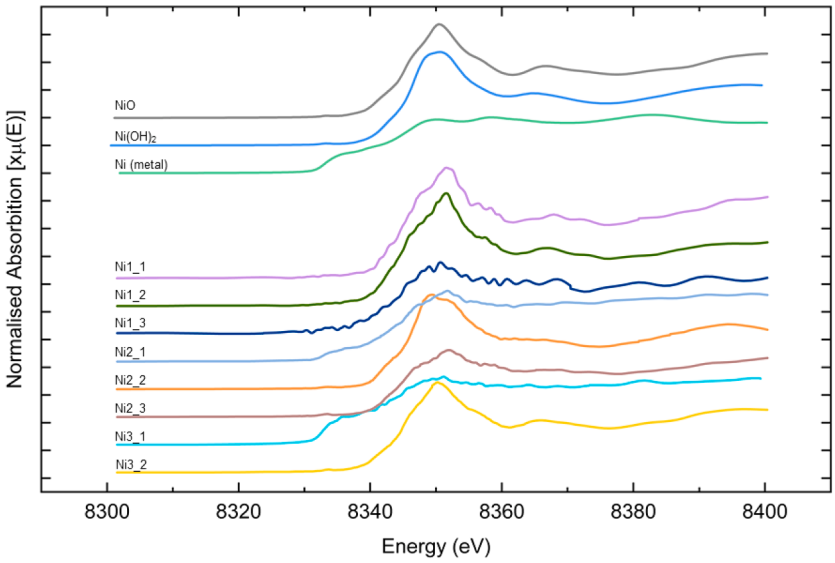

Fig. 8. Normalized Ni XANES spectra of reference materials (top) and collected on various clasts of the BA samples (bottom).

Table 7
Results of the LCF analysis performed on the spectra collected at the Ni K-edge on BA clasts (reported quantities are %; sigmas in brackets).

Compounds	*Ni1_1*	*Ni1_2*	*Ni1_3*	*Ni2_1*	*Ni2_2*	*Ni2_3*	*Ni3_1*	*Ni3_2*
Metal Ni			35 (3)	66 (2)		28 (11)	84 (5)	
NiO	17 (10)	40 (16)	13 (10)	34 (16)		49 (9)	16 (20)	67 (7)
Ni(OH)$_2$	83 (10)	60 (12)	52 (14)		100	23 (8)		33 (4)

and lime. Some of the mineralogical phase in which Pb has been observed in this study are easily leachable, and consequently, a careful evaluation of their intended use is recommended.

In previous works, Cr is commonly found in a stable glass or oxide form. Cr weathering phases were not detected, except for a possible presence in the ettringite structure, as demonstrated only by Piantone et al. (2004). Here, Cr, at higher concentration, is typically found as oxides, like spinel chromite or an Al-Fe-Cr oxide. While in lower concentration, Cr occurs in glasses and no correlation with sulphates was detected. No evidence of Cr VI+, that is the more toxic, carcinogenic and chemical pollutant oxidation state, was found.

For what concerns Ni, no indications about its speciation was found in the literature. We found Ni as a metal or in spinel solid solution together with Cr and Fe. However, it appears to be more prone to alteration than Cr, forming Ni-bearing oxides and hydroxides.

Last, Zn is one of the most mobile PTE; its presence poses environmental concern (Borah et al., 2020). Elevated Zn concentrations in aquatic environments, can impact growth, reproduction, and overall health of aquatic organisms. In soil, excessive Zn content can disrupt microbial communities and affect nutrient cycling, leading to adverse effects on plant growth and soil fertility. In BA Zn is found in a wide range of different phases reported in Table 8: $Zn_2P_2O_7$, $Zn_3(PO_4)_2 \cdot 4H_2O$ or $Zn_2PO_4(OH)$ were found by a single author by XRD (Crannell et al., 2000; Piantone et al., 2004), assumingly in significant amount, but were not confirmed by other authors. In Meima and Comans (1999) as much as 26 % of the examined particles contained Zn in metal form, while in none of the investigated samples in this study, metal Zn was found. Moreover, the high-temperature Zn-phases as zincite, willemite and spinels (franklinite and gahnite) are also commonly encountered. Zn is reported as an impurity in other oxides, silicate glasses, feldspars, and pyroxenes (Table 8). The alteration products as nanosized grains found by XAS analyses include hydrated silicate, hydroxides, carbonates and chlorides. In this work, Zn is present in various phases, some identified by SEM-EDS, while others are found in close proximity within a single $50 \times 50 \mu m^2$ area, and were identified through XANES spectral deconvolution. Zn is observed in silicates like willemite, hardystonite or hemimorphite, as well as in oxides and hydroxides, like gahnite spinel and zincite, in the ZnS sulphide, in the very soluble form of $ZnCl_2$ and in carbonates like smithsonite or hydrozincite, that can be an alteration product of hemimorphite. Moreover, the presence of Zn in a silicate glass is suggested by a locally enriched regions as revealed by SEM-EDS. Zn was not found in sulphates or as a metal. The complex mineralogy of Zn results in equally complex leaching behaviour depending of: a) degree of weathering and consequently ratio between high temperature and alteration phases; b) grain size, which may affect the solubility; c) mineralogical species of the weathering phases, which are specific of each WtE plants.

These results indicate that each WtE plant has its own specific mineralogy, requiring a tailored investigation for any use of the BA. Nevertheless, upon comparison with different WtE plants, some common mineralogical phases hosting PTE can be identified.

4.2. Speciation and leaching

Prediction of leaching behaviour in a complex system like BA involves the phases within the ashes, their proportion, and their thermodynamic properties in multiple equilibria. A problem in the characterization of this material is that no equilibrium condition is present globally but only at a local microscale; moreover, the thermodynamic properties of several minerals, either in terms of modelling the host solid solution, or for the properties of the amorphous materials, are lacking. In previous investigation it was shown that the glass, which is the main constituent of the BA, is not a unique phase with its own thermodynamic properties, but that there are several glasses, with different composition and assumingly different thermodynamic behaviour. The different glasses have compositions loosely falling within the $CaO\text{-}Al_2O_3\text{-}SiO_2$ field, but they may differ by K and Na content, by Fe and possibly organic dispersed matter, and last, by the content in PTE

Table 8
Cu, Zn, Cr, Pb, Ni and Co species found in literature data (ref, in brackets) and implemented with data of this work.

Element	Suggested form/Mineral	Technique	References
Copper	*CuO (tenorite)*	TEM, SEM-EDS + XRD	(Meima and Comans, 1999)
		XRD, EPMA	(Bayuseno and Schmahl, 2010)
		SEM-EDS	(Wei et al., 2011b)
		XANES + EXAFS	(Lassesson and Steenari, 2013)
		XANES + EXAFS	(Olsson et al., 2009)
		XANES	(Rissler et al., 2020)
		EXAFS	(Tiberg et al., 2021)
		XANES	this work
	Cu_2O (cuprite)	XRD	(Meima and Comans, 1999)
		XANES + EXAFS	(Lassesson and Steenari, 2013)
		XANES	(Rissler et al., 2020)
		XANES	this work
	$Cu_2(OH)_3Cl$ (atacamite/ paratacamite)	XRD	(Piantone et al., 2004)
	$Cu(OH)_2$	XANES	(Rissler et al., 2020)
	$CuSiO_3 \cdot H_2O$	XANES	(Rissler et al., 2020)
	$Cu_{19}Cl_4SO_4(OH)_{32} \cdot 3H_2O$ (connellite)	XRD	(Piantone et al., 2004)
	$Cu_2Zn_4Al_2(OH)_{16}CO_3 \cdot 4H_2O$	XRD	(Piantone et al., 2004)
	Cu_2S	XRD	(Bayuseno and Schmahl, 2010)
	CuS	XRD	(Bayuseno and Schmahl, 2010)
	$Cu_{11}(OH)_{14}(CrO_4)_4$	XRD	(Piantone et al., 2004)
	$CuCr_2O_4$	XANES + EXAFS	(Lassesson and Steenari, 2013)
		XANES	(Rissler et al., 2020)
	$CuFe_2O_4$	XANES	(Rissler et al., 2020)
	Cu metal (or alloy)	SEM-EDS	(Meima and Comans, 1999)
		XANES + EXAFS	(Lassesson and Steenari, 2013)
		SEM-EDS	(Wei et al., 2011b)
		XANES	(Rissler et al., 2020)
		SEM-EDS	(Mantovani et al., 2021)
		EXAFS	(Tiberg et al., 2021)
		SEM EDS + XANES	this work
	$Cu_2(OH)_2CO_3$ (malachite)	Geochemical model	(Dijkstra et al., 2006)
		XANES	(Rissler et al., 2020)
	Cu adsorption to Fe/Al-hydroxides	Geochemical model	(Meima and Comans, 1999)
		Geochemical model	(Dijkstra et al., 2006)
	Cu substitution in different minerals	SEM-EDS + XRD	(Meima and Comans, 1999)
Zinc	*ZnO (zincite)*	Crystal-chemical data and XRD	(Piantone et al., 2004)
		XRD + SEM-EDS	(Piantone et al., 2004)
		XANES + EXAFS	(Steenari and Norén, 2008)
		XANES	(Rissler et al., 2020)
		EXAFS	(Tiberg et al., 2021)
		SEM-EDS + XANES	this work
	ZnS	XANES	this work
	$ZnCl_2$	XANES	(Rissler et al., 2020)
		XANES	this work
	$ZnCO_3$ (smithsonite)	XANES	(Rissler et al., 2020)
		XANES	this work
	$Zn_2P_2O_7$	XRD	(Tang et al., 2015)
	$Zn_2(PO_4)(OH)$ (descloizite)	XRD	(Piantone et al., 2004)
	$Mn_2Zn(PO_4)_2$	XRD	(Crannell et al., 2000)
	$Zn_3(PO_4)_2$	XRD	(Crannell et al., 2000)
		XANES	(Rissler et al., 2020)
		XANES	this work
	$Zn_3(PO_4)_2 \cdot 4H_2O$	XRD	(Crannell et al., 2000)
	$ZnFe_2O_4$ (franklinite)	XANES	(Rissler et al., 2020)
		EXAFS	(Tiberg et al., 2021)
		XANES	this work
	$ZnFe_2(SO_4)_4$ (lishizhenite)	XRD	(Piantone et al., 2004)
	$ZnAl_2O_4$ (gahnite)	XANES	(Rissler et al., 2020)
		EXAFS	(Tiberg et al., 2021)
		SEM - EDS + XANES	this work
	Zn_2AlO_7	SEM-EDS	this work
	Ca_2ZnSiO_7 (hardystonite)	SEM-EDS	this work
	Zn_2SiO_4 (willemite)	Geochemical model	(Dijkstra et al., 2006)
		XANES + EXAFS	(Steenari and Norén, 2008)
		XANES	(Rissler et al., 2020)
		EXAFS	(Tiberg et al., 2021)
		SEM-EDS	this work
	$Zn_4Si_2O_7(OH)_2 \cdot (H_2O)$ (hemimorfite)	XANES	(Rissler et al., 2020)
		EXAFS	(Tiberg et al., 2021)
		XANES	this work
	$Zn(OH)_2$	XANES + EXAFS	(Steenari and Norén, 2008)
		EXAFS	(Tiberg et al., 2021)
	$Zn_5(CO_3)_2(OH)_6$ (hydrozincite)	XANES	(Rissler et al., 2020)

(*continued on next page*)

Table 8 (*continued*)

Element	Suggested form/Mineral	Technique	References
		SEM-EDS	(Meima and Comans, 1999)
	Zn metal (or alloy)	SEM-EDS	(Meima and Comans, 1999)
		SEM - EDS	(Wei et al., 2011b)
		XANES	(Rissler et al., 2020)
	Zn adsorption to or surface precipitates on Fe/Al-hydroxides	Geochemical model	(Meima and Comans, 1999)
		Geochemical model	(Dijkstra et al., 2006)
	Zn sunstituition in spinel crystals	SEM - EDS	(Wei et al., 2011b)
		SEM-EDS	(Mantovani et al., 2021)
	Zn substitution in calcite	Mapping by microprobe	(Piantone et al., 2004)
	Zn substitution in Fe oxides/ oxyhydroxides	Mapping by microprobe	(Piantone et al., 2004)
	Zn substitution in ettringite	Mapping by microprobe	(Piantone et al., 2004)
	Zn in solid solution with carbonates	Mapping by microprobe	(Piantone et al., 2004)
Chromium	$FeCrO_3$	SEM-EDS	this work
	$FeCr_2O_4$	SEM-EDS + XANES	this work
	$Ca_6Cr_2(SO_4)_3(OH)_{12}\cdot H_2O$ *(bentorite)*	XRD	(Piantone et al., 2004)
	Cr substitution in spinel crystal	SEM - EDS	(Wei et al., 2011b)
		SEM - EDS	(Mantovani et al., 2021)
	Cr in ettringite	XRD	(Piantone et al., 2004)
	Cr in glass matrix	SEM - EDS	this work
	Ca_2PbO_4	SEM-EDS	this work
Lead	$PbCO_3$	Geochemical model	(Meima and Comans, 1999)
		XANES	this work
	Pb_3O_4	SEM-EDS	this work
	$PbCrO_4$ *(crocoïte)*	XRD	(Piantone et al., 2004)
	$Pb_4Cu_4O_4Cl_8\cdot 5H_2O$ *(cumingite)*	XRD	(Piantone et al., 2004)
	Pb substitution in calcite	Mapping by microprobe	(Piantone et al., 2004)
	Pb substitution in Fe oxides/ oxyhydroxides	Mapping by microprobe	(Piantone et al., 2004)
	Pb substitution in ettringite	Mapping by microprobe	(Piantone et al., 2004)
	Pb substituition in spinel crystal	SEM - EDS	(Wei et al., 2011b)
	Pb substituion in TiO_2	SEM - EDS	this work
	Pb metal (or alloy)	SEM - EDS	(Meima and Comans, 1999)
		SEM - EDS	(Wei et al., 2011b)
Nickel	*NiO*	XANES	this work
	$Ni(OH)_2$	XANES	this work
	Ni (metal or alloy)	XANES	this work
Cobalt	*CoO*	XANES + SEM - EDS	this work
	Co (metal or alloy)	XANES + SEM - EDS	this work

(Mantovani et al., 2021). A major problem is the coexistence of a heterogeneous material in which connection between the different grains is not granted; moreover, weathering which occurs at the rim of the grains promotes further local complexity. This may lead to significant differences between each WtE plants in terms of PTE leaching. In fact, as reported in Mantovani et al., (2023), for BA sampled in five different WtE plants in northern Italy and subjected to leaching tests (following UNI EN-12457-2), a different release of PTE was recorded despite a very similar chemical composition for both major and minor elements. Between WtE plants the leached fraction diverges by one order of magnitude for Cr (4 -458 μg/l), Ni (2–57 μg/l), Pb (0–59 μg/l) and Zn (0–0.12 mg/l), and by two orders of magnitude for Cu (0.05–5.31 mg/l) (Mantovani et al., 2023). The PTE leached from the 0.5-1 mm grain size of the Parma WtE plant (the same grain size taken into account in this work) are compared with the bulk mineralogical composition. Due the pH of the leaching (pH = 7) the released fraction would involve only very soluble phases. A sequential extraction procedure (SEP) reported by Alam et al. (2019) showed that Zn is among PTE the most leachable, a result which was confirmed by preliminary SEP data on Parma BA (De Matteis, 2023). Leaching promotes an almost complete solubilisation of Cl, which is released by 70 % (Mantovani et al., 2023). We may assume that only minor content of Cl is locked within a glass or in some stable crystal forms, while the most amount of Cl is present as highly soluble phases (i. e. chlorides, ettringite, etc.). Highly soluble Cu-chlorides may therefore account for the leached Cu. In the case of Ni, no evidence of Ni chlorides was found, but a wider transformation in hydroxide could account for the leached Ni. Pb was found in insoluble oxides and carbonates. The higher concentration of Cr in leachate is puzzling: Cr was invariably found in phases highly stable, like in chromite, or in metals. A possible suggestion, although with no evidence in the investigation, may come from dissolution of Cr in ettringite as CrO_4^{2-} replacing SO_4^{2-} (Song et al., 2019). What emerges from this work is the significant heterogeneity of the BA concerning their chemical-mineralogical composition and leaching behaviour. The data here presented regard to a specific particle size from a particular WtE plant. It would be desirable to characterize different BA using a multi-technique approach to gather more information about the variability of the PTE hosting phases. It would be necessary to implement this data for a safe reuse of these materials and for predict potential environmental damage.

5. Conclusions

The PTE distribution and speciation (Pb, Cr, Cu, Zn, Co and Ni) has been investigated and determined using complementary techniques. The main results are:

1) For each grain, the presence of a core and rim structures were typically observed. The core is characterized by high-temperature phases, mixed with glass of varying composition that is in local equilibrium. Differently, the rim is composed of finely grained carbonates, sulphates, oxides, hydroxides, chlorides, and organic residual materials, likely originating from weathering processes:
2) Among PTE, Zn and Cu are present at the grain rims, whereas the others are generally found in the core;
3) The speciation of Cu and Ni involves the transformation from metal to oxide and hydroxide. Cu shows also the coexistence of Cu I+ intermediate oxidation state;
4) Pb is generally found in carbonates or in oxides; Zn has a wide mineralogical speciation, in carbonates, oxides and silicates;
5) Cr is found in insoluble oxides, and never in Cr VI+ oxidation state. The results from leaching experiments however suggest that wider solubility might be achieved by some neglected contribution of Cr III+ exchanging with Al or of Cr VI+ exchanging with S in SO_4^{2-} in the highly soluble ettringite;
6) Due to different waste input, combustion temperature, local equilibria, grain size and ageing, the speciation of PTE occurs in a wide range of minerals; these variables affect the elements leaching, and the predictions of the potential leaching results obtained for one WtE plant should be extended to others with extreme care.

Funding

This research has been financially supported by the program "FIL – Quota Incentivante" of University of Parma and PRIN 2017 2017L83S77_005 "Mineral reactivity, a key to understand large- scale processes: from rock forming environments to solid waste recovering/ lithification". In addition, this work has benefited from the equipment and framework of the COMP-HUB Initiative, funded by the "Departments of Excellence" program of the Italian Ministry for Education, UNIVERSITY AND RESEARCH (MIUR 2018-2022). This research is part of the project NODES which has received funding from the MUR – M4C2 1.5 of PNRR with grant agreement no.ECS00000036

CRediT authorship contribution statement

C. De Matteis: Methodology, Data curation, Investigation, Writing – original draft, Writing – review & editing, Validation. **S. Pollastri:** Methodology, Investigation, Data curation. **L. Mantovani:** Data curation, Writing – review & editing, Funding acquisition, Supervision. **M. Tribaudino:** Conceptualization, Data curation, Writing – original draft, Validation, Funding acquisition, Supervision.

Declaration of Competing Interest

The authors declare that they have no known competing financial interests or personal relationships that could have appeared to influence the work reported in this paper.

Data availability

Data will be made available on request.

Acknowledgements

Thanks are due to **Andrea Comelli** from University of Parma who provided the stab, **Roberto Cossio** from University of Torino for assistance in SEM-EDS analysis. In addition, we would like to thank the **ELETTRA XRF beamline group** for beamtime, assistance and helpful advices.

Supplementary materials

Supplementary material associated with this article can be found, in the online version, at doi:10.1016/j.envadv.2023.100453.

References

Abramov, S., He, J., Wimmer, D., Lemloh, M.L., Muehe, E.M., Gann, B., Roehm, E., Kirchhof, R., Babechuk, M.G., Schoenberg, R., Thorwarth, H., Helle, T., Kappler, A., 2018. Heavy metal mobility and valuable contents of processed municipal solid waste incineration residues from Southwestern Germany. Waste Manag. 79, 735–743. https://doi.org/10.1016/j.wasman.2018.08.010.

Alam, Q., Schollbach, K., van Hoek, C., van der Laan, S., de Wolf, T., Brouwers, H.J.H., 2019. In-depth mineralogical quantification of MSWI bottom ash phases and their association with potentially toxic elements. Waste Manag. 87, 1–12. https://doi.org/10.1016/j.wasman.2019.01.031.

Ambiente, I., 2022. Dichiarazione Ambientale 2021 Polo Ambientale Integrato di Parma.

Aminiyan, M.M., Baalousha, M., Mousavi, R., 2018. The ecological risk, source identification, and pollution assessment of heavy metals in road dust : a case study in Rafsanjan, SE Iran 13382–13395. Environ. Sci. Pollut. Res. https://doi.org/10.1007/s11356-017-8539-y.

ANPA, 2002. Il nuovo elenco dei rifiuti e gli schemi di trasposizione. Agenzia Nazionale per la Protezione dell. Ambiente.

Assi, A., Bilo, F., Federici, S., Zacco, A., Depero, L.E., Bontempi, E., 2020. Bottom ash derived from municipal solid waste and sewage sludge co-incineration: First results about characterization and reuse. Waste Manag. 116, 147–156. https://doi.org/10.1016/j.wasman.2020.07.031.

Astrup, T., Muntoni, A., Polettini, A., van Gerven, T., van Zomeren, A., 2016. Treatment and Reuse of Incineration Bottom Ash.

Bawab, J., Khatib, J., Kenai, S., Sonebi, M., 2021. A Review on Cementitious Materials Including Municipal Solid Waste Incineration Bottom Ash (MSWI-BA) as Aggregates, pp. 1–19.

Bayuseno, A.P., Schmahl, W.W., 2010. Understanding the chemical and mineralogical properties of the inorganic portion of MSWI bottom ash. Waste Manag. 30, 1509–1520. https://doi.org/10.1016/j.wasman.2010.03.010.

Bertolini, L., Carsana, M., Cassago, D., Curzio, A.Q., Collepardi, M., 2004. MSWI ashes as mineral additions in concrete. Cem. Concr. Res. 34, 1899–1906. https://doi.org/10.1016/j.cemconres.2004.02.001.

Borah, P., Gujre, N., Rene, E.R., Rangan, L., Kumar, R., Karak, T., Mitra, S., 2020. Chemosphere assessment of mobility and environmental risks associated with copper, manganese and zinc in soils of a dumping site around a Ramsar site. Chemosphere 254, 126852. https://doi.org/10.1016/j.chemosphere.2020.126852.

Bourtsalas, A., Vandeperre, L.J., Grimes, S.M., Themelis, N., Cheeseman, C.R., 2014. Production of pyroxene ceramics from the fine fraction of incinerator bottom ash. Waste Manag. 45, 217–225. https://doi.org/10.1016/j.wasman.2015.02.016.

Cai, X., Huang, Q.X., Alhadj-Mallah, M.M., Chi, Y., Yan, J.H., 2015. Characterization of zinc vapor condensation in fly ash particles using synchrotron X-ray absorption spectroscopy. J. Zhejiang Univ. Sci. A 16, 70–80. https://doi.org/10.1631/jzus.A1400178.

Caviglia, C., Confalonieri, G., Corazzari, I., Destefanis, E., Mandrone, G., Pastero, L., Boero, R., Pavese, A., 2019. Effects of particle size on properties and thermal inertization of bottom ashes (MSW of Turin's incinerator). Waste Manag. 84, 340–354. https://doi.org/10.1016/j.wasman.2018.11.050.

Chen, L., Liao, Y., Ma, X., Lu, S., 2020. Heavy metals chemical speciation and environmental risk of bottom slag during co-combustion of municipal solid waste and sewage sludge. J. Clean. Prod. 262, 121318 https://doi.org/10.1016/j.jclepro.2020.121318.

Chimenos, J.M., Fernández, A.I., Miralles, L., Segarra, M., Espiell, F., 2003. Short-term natural weathering of MSWI bottom ash as a function of particle size. Waste Manag. 23, 887–895. https://doi.org/10.1016/S0956-053X(03)00074-6.

Choi, Y.G., Kim, K.H., Chernov, V.A., Heo, J., 1999. Pb LIII-edge EXAFS and XANES analyses on the structural environment of lead in PbO-Ga_2O_3 glasses. J. Non. Cryst. Solids 246, 128–135. https://doi.org/10.1016/S0022-3093(99)00010-1.

Crannell, B.S., Eighmy, T.T., Krzanowski, J.E., Eusden, J.D., Shaw, E.L., Francis, C.A., 2000. Heavy metal stabilization in municipal solid waste combustion bottom ash using soluble phosphate. Waste Manag. 20, 135–148. https://doi.org/10.1016/S0956-053X(99)00312-8.

De Matteis, C., 2023. Mineralogical and Chemical Characterization of Bottom Ahes from Waste Incineration. Università di Parma.

De Silva, S., Ball, A.S., Indrapala, D.V, Reichman, S.M., 2021. Chemosphere Review of the interactions between vehicular emitted potentially toxic elements, roadside soils, and associated biota. Chemosphere 263, 128135. https://doi.org/10.1016/j.chemosphere.2020.128135.

Dijkstra, J.J., Comans, R.N.J., Schokker, J., van der Meulen, M.J., 2019. The geological significance of novel anthropogenic materials: deposits of industrial waste and by-products. Anthropocene. https://doi.org/10.1016/j.ancene.2019.100229.

Dijkstra, J.J., Van Der Sloot, H.A., Comans, R.N.J., 2006. The leaching of major and trace elements from MSWI bottom ash as a function of pH and time. Appl. Geochemistry 21, 335–351. https://doi.org/10.1016/j.apgeochem.2005.11.003.

Dubrail, J., Farges, F., Gautron, L., Harfouche, M., Borca, C., Grolimund, D., 2009. Pb in naturally irradiated monazites and zircons. J. Phys. Conf. Ser. 190 https://doi.org/10.1088/1742-6596/190/1/012180.

Eusden, J.D., Eighmy, T.T., Hockert, K., Holland, E., Marsella, K., 1999. Petrogenesis of municipal solid waste combustion bottom ash. Appl. Geochem. 14, 1073–1091. https://doi.org/10.1016/S0883-2927(99)00005-0.

Feng, S., Wang, X., Wei, G., Peng, P., Yang, Y., Cao, Z., 2007. Leachates of municipal solid waste incineration bottom ash from Macao: heavy metal concentrations and genotoxicity. Chemosphere 67, 1133–1137. https://doi.org/10.1016/j.chemosphere.2006.11.030.

Funari, V., Braga, R., Bokhari, S.N.H., Dinelli, E., Meisel, T., 2015. Solid residues from Italian municipal solid waste incinerators: a source for '"critical'" raw materials. Waste Manag. 45, 206–216. https://doi.org/10.1016/j.wasman.2014.11.005.

Goodarzi, F., Huggins, F.E., 2001. Monitoring the species of arsenic, chromium and nickel in milled coal, bottom ash and fly ash from a pulverized coal-fired power plant in western Canada. J. Environ. Monit. 3, 1–6. https://doi.org/10.1039/b006733o.

Gualtieri, A., 2000. Accuracy of XRPD QPA using the combined Rietveld{–}RIR method. J. Appl. Crystallogr. 267–278. https://doi.org/10.1107/S002188989901643X.

Haberl, J., Schuster, M., 2019. Solubility of elements in waste incineration fly ash and bottom ash under various leaching conditions studied by a sequential extraction procedure. Waste Manag. 87, 268–278. https://doi.org/10.1016/j.wasman.2019.02.001.

Hsiao, M.C., Wang, H.P., Chang, J.E., Peng, C.Y., 2006. Tracking of copper species in incineration fly ashes. J. Hazard. Mater. 138, 539–542. https://doi.org/10.1016/j.jhazmat.2006.05.087.

Hsiao, M.C., Wang, H.P., Huang, Y.J., Yang, Y.W., 2001. EXAFS study of copper in waste incineration fly ashes. J. Synchrotron Radiat. 8, 931–933. https://doi.org/10.1107/S0909049500020987.

Hsiao, M.C., Wang, H.P., Wei, Y.L., Chang, J.E., Jou, C.J., 2002. Speciation of copper in the incineration fly ash of a municipal solid waste. J. Hazard. Mater. 91, 301–307. https://doi.org/10.1016/S0304-3894(02)00015-8.

Huber, F., Blasenbauer, D., Aschenbrenner, P., Fellner, J., 2020. Complete determination of the material composition of municipal solid waste incineration bottom ash. Waste Manag. 102, 677–685. https://doi.org/10.1016/j.wasman.2019.11.036.

Inkaew, K., Saffarzadeh, A., Shimaoka, T., 2016. Modeling the formation of the quench product in municipal solid waste incineration (MSWI) bottom ash. Waste Manag. 52, 159–168. https://doi.org/10.1016/j.wasman.2016.03.019.

Izquierdo, M., Querol, X., Bizinotto, M.B., Enric, V., Xavier, Q., Marilda, B., Ángel, L., Felicià, P., 2001. View project Cerro PhD View project Use of Bottom Ash from Municipal Solid Waste Incineration as a Road Material.

Jark, W., Eichert, D., Luehl, L., Gambitta, A., 2014. Optimisation of a compact optical system for the beamtransport at the x-ray fluorescence beamline at Elettra for experiments with small spots. Proc. SPIE 92070G. https://doi.org/10.1117/12.2063009.

Jernejcic, J., Skledar, S., Sencar, J., 1969. Synthesis and characterization of calcium orthoplumbate. Indus. Eng. Chem.-Product Res. Dev. 8, 149–154.

Karydas, A.G., Czyzycki, M., Leani, J.J., Migliori, A., Osan, J., Bogovac, M., Wrobel, P., Vakula, N., Padilla-Alvarez, R., Menk, R.H., Gol, M.G., Antonelli, M., Tiwari, M.K., Caliri, C., Vogel-Mikuš, K., Darby, I., Kaiser, R.B., 2018. An IAEA multi-technique X-ray spectrometry endstation at Elettra Sincrotrone Trieste: Benchmarking results and interdisciplinary applications. J. Synchrotron Radiat. 25, 189–203. https://doi.org/10.1107/S1600577517016332.

Kaza, S., Yao, L., Bhads-Tata, P., Van Woerden, F., 2018. What a waste. Manager. https://doi.org/10.1680/imuen.2000.32747.

Kitamura, H., Dahlan, A.V., Tian, Y., Shimaoka, T., Yamamoto, T., Takahashi, F., 2020. Application of micro-scale correlation analysis to estimate metal speciation and the matrix in municipal solid waste incineration fly ash. J. Mater. Cycles Waste Manag. 22, 1081–1093. https://doi.org/10.1007/s10163-020-01001-w.

Kostomitsopoulou Marketou, A., Giannici, F., Handberg, S., De Nolf, W., Cotte, M., Caruso, F., 2021. Synchrotron radiation-based micro-XANES and micro-XRF study of unsuccessfully produced Egyptian blue from the late Hellenistic production site of Kos (Dodecanese, Greece). Anal. Chem. 93, 11557–11567. https://doi.org/10.1021/acs.analchem.1c02063.

Lassesson, H., Steenari, B.M., 2013. Speciation of copper in ash from a fluidized-bed boiler fired with municipal solid waste. Energy Fuels 27, 3891–3897. https://doi.org/10.1021/ef400386j.

Lei, K., Giubilato, E., Critto, A., Pan, H., Lin, C., 2016. Contamination and human health risk of lead in soils around lead/zinc smelting areas in China. Environ. Sci. Pollut. Res. 13128–13136. https://doi.org/10.1007/s11356-016-6473-z.

Liu, P., Ptacek, C.J., Blowes, D.W., Finfrock, Y.Z., Liu, Y.Y., 2020. Characterization of chromium species and distribution during Cr(VI) removal by biochar using confocal micro-X-ray fluorescence redox mapping and X-ray absorption spectroscopy. Environ. Int. 134, 105216 https://doi.org/10.1016/j.envint.2019.105216.

Loginova, E., Volkov, D.S., van de Wouw, P.M.F., Florea, M.V.A., Brouwers, H.J.H., 2019. Detailed characterization of particle size fractions of municipal solid waste incineration bottom ash. J. Clean. Prod. 207, 866–874. https://doi.org/10.1016/j.jclepro.2018.10.022.

Mantovani, L., De Matteis, C., Tribaudino, M., Boschetti, T., Funari, V., Dinelli, E., Toller, S., Pelagatti, P., 2023. Grain size and mineralogical constraints on leaching in the bottom ashes from municipal solid waste incineration: a comparison of five plants in northern Italy. Front. Environ. Sci. 11, 1–15. https://doi.org/10.3389/fenvs.2023.1179272.

Mantovani, L., Tribaudino, M., De Matteis, C., Funari, V., 2021. Particle size and potential toxic element speciation in municipal solid waste incineration (Mswi) bottom ash. Sustain 13, 1–17. https://doi.org/10.3390/su13041911.

Meima, Jeannet A, Comans, R.N.J., 1999. The leaching of trace elements from municipal solid waste incinerator bottom ash at different stages of weathering. Appl. Geochem. 14, 159–171. https://doi.org/10.1016/S0883-2927(98)00047-X.

Olsson, S., Gustafsson, J.P., Berggren Kleja, D., Bendz, D., Persson, I., 2009. Metal leaching from MSWI bottom ash as affected by salt or dissolved organic matter. Waste Manag. 29, 506–512. https://doi.org/10.1016/j.wasman.2008.03.017.

Pagani, A., Francescon, F., Pavese, A., Diella, V., 2010. Sanitary-ware vitreous body characterization method by optical microscopy, elemental maps, image processing and X-ray powder diffraction. J. Eur. Ceram. Soc. 30, 1267–1275. https://doi.org/10.1016/j.jeurceramsoc.2009.11.008.

Patterson, Clair C., 1965. Contaminated and natural lead environments of man. Arch. Environ. Health 11 (3), 344–360. https://doi.org/10.1080/00039896.1965.10664229.

Piantone, P, Bodénan, F., Chatelet-Snidaro, L., 2004. Mineralogical study of secondary mineral phases from weathered MSWI bottom ash: Implications for the modelling and trapping of heavy metals. Appl. Geochem. 19, 1891–1904. https://doi.org/10.1016/j.apgeochem.2004.05.006.

Pshinko, G.N., Kosorukov, A.A., Puzyrnaya, L.N., Kobets, S.A., 2013. Recovery of U(VI) from aqueous media with layered double hydroxides of Zn and Al, intercalated with complexones. Radiochemistry 55, 601–604. https://doi.org/10.1134/S1066362213060064.

Ravel, B., Newville, M., 2005. ATHENA, ARTEMIS, HEPHAESTUS: data analysis for X-ray absorption spectroscopy using IFEFFIT. J. Synchrotron Radiat. 12, 537–541. https://doi.org/10.1107/S0909049505012719.

Rissler, J., Klementiev, K., Dahl, J., Steenari, B.M., Edo, M., 2020. Identification and quantification of chemical forms of Cu and Zn in MSWI Ashes Using XANES. Energy Fuels 34, 14505–14514. https://doi.org/10.1021/acs.energyfuels.0c02226.

Rohatgi, A., 2014. Web Plot Digitizer 3.9, pp. 1–17. http://arohatgi.info/WebPlotDigitizer.

Santos, R.M., Mertens, G., Salman, M., Cizer, Ö., Van Gerven, T., 2013. Comparative study of ageing, heat treatment and accelerated carbonation for stabilization of municipal solid waste incineration bottom ash in view of reducing regulated heavy metal/metalloid leaching. J. Environ. Manage. 128, 807–821. https://doi.org/10.1016/j.jenvman.2013.06.033.

Sharma, A., Yoo, S.I., 2018. Subsolidus phase relationships in the Al2O3–SnO2–ZnO ternary system at 1200°C in air. J. Alloys Compd. 740, 536–540. https://doi.org/10.1016/j.jallcom.2017.10.160.

Shevchenko, M., Jak, E., 2019. Experimental liquidus study of the ternary CaO-ZnO-SiO_2 system. Metall. Mater. Trans. B. 50, 2780–2793. https://doi.org/10.1007/s11663-019-01709-7.

Song, Y., Li, J., Peng, M., Deng, Z., Yang, J., Liu, W., Shi, Z., Lin, Z., 2019. Identification of Cr(VI) speciation in ferrous sulfate-reduced chromite ore processing residue (rCOPR) and impacts of environmental factors erosion on Cr(VI) leaching. J. Hazard. Mater. 373, 389–396. https://doi.org/10.1016/j.jhazmat.2019.03.097.

Steenari, B.-M., Norén, K., 2008. Speciation of Zinc in Ash Investigated by X-Ray Absorption Spectroscopy 50.

Stigliani, W.M., Doelman, P., Salomons, W., Schulin, R., Gera, R.B., Zee, S.E.A.T.M.Van Der, Stigliani, B.W.M., Doelman, P., Salomons, W., Schulin, R., Smidt, G.R.B., Zee, S.E.A.T.M.Van Der, 2010. Environment : Science and Policy for Sustainable Development Chemical Time Bombs : Predicting the Unpredictable, pp. 37–41.

Suzuki, R.O., Nagata, J.I., Risold, D., 1998. Experimental phase equilibria in the PbOx-CaO system. J. Am. Ceram. Soc. 81, 2493–2496. https://doi.org/10.1111/j.1151-2916.1998.tb02651.x.

Šyc, M., Simon, F.G., Hykš, J., Braga, R., Biganzoli, L., Costa, G., Funari, V., Grosso, M., 2020. Metal recovery from incineration bottom ash: state-of-the-art and recent developments. J. Hazard. Mater. https://doi.org/10.1016/j.jhazmat.2020.122433.

Tang, P., Florea, M.V.A., Spiesz, P., Brouwers, H.J.H., 2015. Characteristics and application potential of municipal solid waste incineration (MSWI) bottom ashes from two waste-to-energy plants. Constr. Build. Mater. 83, 77–94. https://doi.org/10.1016/j.conbuildmat.2015.02.033.

Tiberg, C., Sjöstedt, C., Karlfeldt Fedje, K., 2021. Speciation of Cu and Zn in bottom ash from solid waste incineration studied by XAS, XRD, and geochemical modelling. Waste Manag. 119, 389–398. https://doi.org/10.1016/j.wasman.2020.10.023.

Toby, B.H., Von Dreele, R., 2013. GSAS-II: the genesis of a modern open-source all purpose crystallography software package. J. Appl. Crystallogr. 544–549. https://doi.org/10.1107/S0021889813003531.

Tribaudino, M., Vollprecht, D., Pavese, A. (Eds.), 2023. Minerals and Waste. Springer, Nature.

Wang, S.J., He, P.J., Shao, L.M., Zhang, H., 2016. Multifunctional effect of Al_2O_3, SiO_2 and CaO on the volatilization of PbO and $PbCl_2$ during waste thermal treatment. Chemosphere 161, 242–250. https://doi.org/10.1016/j.chemosphere.2016.07.020.

Wei, Y., Mei, X., Shi, D., Liu, G., Li, L., Shimaoka, T., 2017. Separation and characterization of magnetic fractions from waste-to-energy bottom ash with an emphasis on the leachability of heavy metals. Environ. Sci. Pollut. Res. 24, 14970–14979. https://doi.org/10.1007/s11356-017-9145-8.

Wei, Y., Shimaoka, T., Saffarzadeh, A., Takahashi, F., 2011a. Alteration of municipal solid waste incineration bottom ash focusing on the evolution of iron-rich constituents. Waste Manag. 31, 1992–2000. https://doi.org/10.1016/j.wasman.2011.04.021.

Wei, Y., Shimaoka, T., Saffarzadeh, A., Takahashi, F., 2011b. Mineralogical characterization of municipal solid waste incineration bottom ash with an emphasis on heavy metal-bearing phases. J. Hazard. Mater. 187, 534–543. https://doi.org/10.1016/j.jhazmat.2011.01.070.

Wrobel, P.M., Bogovac, M., Sghaier, H., Leani, J.J., Migliori, A., Padilla-Alvarez, R., Czyzycki, M., Osan, J., Kaiser, R.B., Karydas, A.G., 2016. LabVIEW interface with Tango control system for a multi-technique X-ray spectrometry IAEA beamline end-station at Elettra Sincrotrone Trieste. Nucl. Instruments Methods Phys. Res. Sect. A 833, 105–109. https://doi.org/10.1016/j.nima.2016.07.030.

Xu, D., Yan, B., Chen, T., Lei, C., Lin, H., 2017. Contaminant characteristics and environmental risk assessment of heavy metals in the paddy soils from lead (Pb)-zinc (Zn) mining areas in Guangdong Province, South China. Environ. Sci. Pollut. Res. 24387–24399. https://doi.org/10.1007/s11356-017-0052-9.

Yao, J., Li, W.B., Kong, Q., Xia, F., Shen, D.S., 2012. Effect of weathering on the mobility of zinc in municipal solid waste incinerator bottom ash. Fuel 93, 99–104. https://doi.org/10.1016/j.fuel.2011.11.026.

Zevenbergen, C., Reeuwijk, L.P.Van, Bradley, J.P., Comans, R.N.J., Schuiling, R.D., 1998. Weathering of MSWI bottom ash with emphasis on the glassy constituents. J. Geochem. Explor. 62, 293–298. https://doi.org/10.1016/S0375-6742(97)00033-2.

Zhu, F., Xiong, Y., Wang, Y., Wei, X., Zhu, X., Yan, F., 2018. Heavy metal behavior in "Washing-Calcination-Changing with Bottom Ash" system for recycling of four types of fly ashes. Waste Manag. 75, 215–225. https://doi.org/10.1016/j.wasman.2018.01.032.